OGLE-2016-BLG-1045: A TEST OF CHEAP SPACE-BASED MICROLENS PARALLAXES

I.-G. SHIN[H1,K0], A. UDALSKI[O1,O0], J. C. YEE[H1,K0,S0,F0], S. CALCHI NOVATI[S1,S0], G. CHRISTIE[F1,F0],
AND
R. POLESKI[O1,E1], P. MRÓZ[O1], J. SKOWRON[O1], M. K. SZYMAŃSKI[O1], I. SOSZYŃSKI[O1], P. PIETRUKOWICZ[O1], S. KOZŁOWSKI[O1],
K. ULACZYK[O1,O2], M. PAWLAK[O1]
(OGLE COLLABORATION),
T. NATUSCH[F2,F1], R. W. POGGE[E1],
(μFUN COLLABORATION),
A. GOULD[K1,E1,E2], C. HAN[K5], M. D. ALBROW[K3], S.-J. CHUNG[K1,K2], K.-H. HWANG[K1], Y.-H. RYU[K1], Y. K. JUNG[H1], W. ZHU[E1],
C.-U. LEE[K1,K2], S.-M. CHA[K1,K4], D.-J. KIM[K1], H.-W. KIM[K1,K2], S.-L. KIM[K1,K2], Y. LEE[K1,K4], D.-J. LEE[K1], B.-G. PARK[K1,K2],
(KMTNET GROUP),
C. BEICHMAN[S2], G. BRYDEN[S3], S. CAREY[S4], B. S. GAUDI[E1], C. B. HENDERSON[S3,N0], Y. SHVARTZVALD[S3,N0]
(*Spitzer* TEAM)

[H1]Harvard-Smithsonian Center for Astrophysics, 60 Garden St., Cambridge, MA 02138, USA
[O1]Warsaw University Observatory, Al. Ujazdowskie 4, 00-478 Warszawa, Poland
[O2]Department of Physics, University of Warwick, Gibbet Hill Road, Coventry CV4 7AL, UK
[F1]Auckland Observatory, Auckland, New Zealand
[F2]Institute for Radio Astronomy and Space Research (IRASR), AUT University, Auckland, New Zealand
[K1]Korea Astronomy and Space Science Institute, 776 Daedeokdae-ro, Yuseong-Gu, Daejeon 34055, Korea
[K2]Korea University of Science and Technology, 217 Gajeong-ro, Yuseong-gu, Daejeon 34113, Korea
[K3]University of Canterbury, Department of Physics and Astronomy, Private Bag 4800, Christchurch 8020, New Zealand
[K4]School of Space Research, Kyung Hee University, Giheung-gu, Yongin, Gyeonggi-do, 17104, Korea
[K5]Department of Physics, Chungbuk National University, Cheongju 28644, Korea
[S1] IPAC, Mail Code 100-22, California Institute of Technology, 1200 E. California Boulevard, Pasadena, CA 91125, USA
[S2] NASA Exoplanet Science Institute, California Institute of Technology, Pasadena, CA 91125, USA
[S3] Jet Propulsion Laboratory, California Institute of Technology, 4800 Oak Grove Drive, Pasadena, CA 91109, USA
[S4] Spitzer Science Center, MS 220-6, California Institute of Technology, Pasadena, CA, USA
[E1]Department of Astronomy, Ohio State University, 140 W. 18th Ave., Columbus, OH 43210, USA
[E2]Max-Planck-Institute for Astronomy, Königstuhl 17, 69117 Heidelberg, Germany

Draft version January 3, 2018

ABSTRACT

Microlensing is a powerful and unique technique to probe isolated objects in the Galaxy. To study the characteristics of these interesting objects based on the microlensing method, measurement of the microlens parallax is required to determine the properties of the lens. Of the various methods to measure microlens parallax, the most robust way is to make simultaneous ground- and space-based observations, i.e., by measuring the space-based microlens parallax. However, space-based campaigns usually require "expensive" resources. Gould & Yee (2012) proposed an idea called the "cheap space-based microlens parallax" that can measure the lens-parallax using only 2 or 3 space-based observations of high-magnification events. This cost-effective observation strategy to measure microlens parallaxes could be used by space-borne telescopes to build a complete sample for studying isolated objects. This would enable a direct measurement of the mass function including both extremely low-mass objects and high-mass stellar remnants. However, to adopt this idea requires a test to check how it would work in actual situations. Thus, we present the first practical test of the idea using the high-magnification microlensing event OGLE-2016-BLG-1045, for which a subset of *Spitzer* observations fortuitously duplicate the prescription of Gould & Yee (2012). From the test, we confirm that the measurement of the lens-parallax adopting this idea has sufficient accuracy to determine the physical properties of the isolated lens.

Subject headings: gravitational lensing: micro – stars: fundamental parameters

1. INTRODUCTION

Isolated objects with various masses such as free-floating planets, brown dwarfs, and black holes are very interesting targets (or potential targets) of study. At the low-mass end, free-floating planets and brown dwarfs may represent the low-mass tail of star formation or the result of bodies ejected during planet formation. Larger-mass objects ($\gtrsim$ several Jupiter masses) have been found with direct imaging in star-forming regions (e.g., Bihain et al. 2009; Esplin & Luhman 2017), and there exist several scenarios to explain their origin and evolution depending on various environmental factors (Whitworth et al. 2007). Microlensing has also probed the free-floating planet population, but with contradictory results. Sumi et al. (2011) argued that Jupiter-mass free-floating planets are about twice as numerous as stars, but Mróz et al. (2017a) did not find any evidence for such a population. At the same time, Mróz et al. (2017a,b) discovered several candidates for less massive (few Earth-mass) free-floating plan-

[O0] OGLE Collaboration
[F0] μFUN Collaboration
[K0] KMTNet Group
[S0] *Spitzer* Team
[N0] NASA Postdoctoral Program Fellow

ets. These lower mass objects could be candidates for ejection from forming planetary systems (e.g., Jurić & Tremaine 2008; Chatterjee et al. 2008; Barclay et al. 2017).

At the high-mass end, there is tension between theoretical predictions of the stellar remnant distribution and the observed population inferred from close binaries. Fryer et al. (2012) predict a smooth distribution of remnant masses ranging from neutron stars to the most massive stellar mass black holes. In contrast, Özel et al. (2012) find a distinct gap between the neutron star and black hole populations in the interval from $\sim 2 - 5\ M_\odot$. Because the only confirmed black holes are found in binary systems, it is unclear whether this feature (and this conflict between observation and theory) is intrinsic to the mass distribution or somehow specific to stellar remnants in close binaries.

Observations of isolated objects spanning the full mass function are necessary to resolve these issues. Despite the interest of these objects, their discovery and study are challenging because they are generally too faint to find (or they may be entirely dark). Moreover, they have no interaction with other stellar objects. Compared to other methods, the microlensing technique is a powerful and unique tool to probe these isolated objects because the technique can in principle detect any object that approaches or aligns with the line of sight between a background star (source) and observer(s), regardless of the brightness of the objects (lenses).

Unfortunately, microlensing observations do not, by themselves, routinely measure the microlens mass, M. Rather, they usually return only the Einstein timescale $t_{\rm E}$, which is a combination of several physical properties of the lens-source system

$$t_{\rm E} \equiv \frac{\theta_{\rm E}}{\mu_{\rm rel}};\ \ \theta_{\rm E} \equiv \sqrt{\kappa M \pi_{\rm rel}};\ \ \kappa \equiv \frac{4G}{c^2\,{\rm au}} \simeq 8.14\,\frac{\rm mas}{M_\odot}. \qquad (1)$$

Here, $(\pi_{\rm rel}, \boldsymbol{\mu}_{\rm rel})$ are the lens-source relative (parallax, proper motion) and $\mu_{\rm rel} = |\boldsymbol{\mu}_{\rm rel}|$. Equation (1) implies that to determine the mass M of dark (or at least, unseen) lenses, requires the measurement of both the Einstein radius $\theta_{\rm E}$ and the scalar amplitude $\pi_{\rm E} = |\boldsymbol{\pi}_{\rm E}|$ of the vector microlens parallax

$$\boldsymbol{\pi}_{\rm E} \equiv \frac{\pi_{\rm rel}}{\theta_{\rm E}}\frac{\boldsymbol{\mu}_{\rm rel}}{\mu_{\rm rel}};\ \ M = \frac{\theta_{\rm E}}{\kappa\pi_{\rm E}};\ \ \pi_{\rm rel} = \theta_{\rm E}\pi_{\rm E}. \qquad (2)$$

According to Equation (2), the microlens parallax quantifies the lens-source vector displacement as seen from different observers' positions, relative to the size of the angular Einstein ring radius. The displacements can be caused by the annual motion of Earth (the annual microlens parallax (APRX; Gould 1992), different locations of observatories, such as Earth compared to space-borne telescopes (the space-based microlens parallax (SPRX; Refsdal 1966), or different ground-based sites (the terrestrial microlens parallax (TPRX; Gould 1997).

These different methods of measuring microlens parallaxes each have their own limitations. The APRX method requires enough time for the motion of Earth to displace the observer's position from rectilinear motion enough to measure the parallax. As a result, the APRX can be measured for long timescale events with timescales $t_{\rm E} \gtrsim 30$ days in favorable cases, but usually $t_{\rm E} \gtrsim 60$ days. However, these long timescale events are not common. Moreover, from Equations (1) and (2), this method can almost never be applied to low-mass lenses. For the TPRX, the displacement can be provided by a combination of simultaneous observations from ground-based telescopes that are well separated. However, because the size of Earth is only a tiny fraction of the projected Einstein ring on the observer plane ($R_\oplus \ll \tilde{r}_{\rm E} \equiv {\rm au}/\pi_{\rm E}$), this measurement can be made for only a few special cases, i.e., extremely magnified lensing events, for which the strongly divergent magnification pattern is very sensitive to small changes in position. Thus, unfortunately, the chance for TPRX measurements would be extremely rare (Gould & Yee 2013).

The SPRX is in principle the most robust way to measure the microlens parallax because the displacement of the space-based observatory from the Earth can easily be a significant fraction of the Einstein ring, e.g., *Spitzer* is ~ 1.3 au from Earth compared to a typical value of $\tilde{r}_{\rm E} \sim 10$ au. Refsdal (1966) already proposed this method a half century ago, and Dong et al. (2007) made the first such measurement. Beginning in 2014, the *Spitzer* satellite has observed more than 500 microlensing events with this aim, yielding almost 80 published microlens parallaxes (Bozza et al. 2016; Calchi Novati et al. 2015a; Chung et al. 2017; Han et al. 2016, 2017; Poleski et al. 2016; Ryu et al. 2017; Shin et al. 2017; Shvartzvald et al. 2015, 2016, 2017; Street et al. 2016; Udalski et al. 2015b; Wang et al. 2017; Yee et al. 2015a; Zhu et al. 2015, 2016, 2017). Even though the SPRX can provide a robust opportunity for measuring microlens parallaxes, there still remains an obstacle to regular adoption of the method because space-based observations usually require "expensive" resources.

Gould & Yee (2012) (hereafter, GY12) proposed to measure "cheap space-based microlens parallaxes (cheap-SPRX)" for high-magnification events. They showed that because the lens-source separation (scaled to $\theta_{\rm E}$) u is extremely small near the peak of a high-magnification $A_{\rm max} \gg 1$ event, $u_{0,\oplus} \simeq A^{-1} \to 0$, the magnitude of the SPRX ($\pi_{\rm E}$) is given by

$$\pi_{\rm E} \simeq \frac{\rm au}{D_{\rm sat}} u_{\rm sat} \qquad (3)$$

$$u_{\rm sat} = \sqrt{2[(1-A_{\rm sat}^{-2})^{-1/2} - 1]} \sim A_{\rm sat}^{-1}. \qquad (4)$$

Here, $D_{\rm sat}$ is the known projected (on the plane of the sky) separation to the satellite, e.g., $D_{\rm sat} \simeq 1.3$ au for the *Spitzer* space telescope, and $u_{\rm sat}$ is the position of satellite in the Einstein ring at the exact moment of the peak of the event as seen from Earth. Space-based observations can be used to determine $u_{\rm sat}$ based on $A_{\rm sat}$,

$$A_{\rm sat} = \frac{F_{\rm sat} - F_{\rm base,sat}}{F_{\rm s,sat}} + 1. \qquad (5)$$

The space-based observations provide the $F_{\rm sat}$ (from an observation at the ground-based peak) and $F_{\rm base,sat}$ (from an observation at "baseline", i.e., well after the event), and ground-based observations can be used to constrain the source $F_{\rm s,sat}$ through color-constraints (Calchi Novati et al. 2015b; Gould et al. 2010). Hence, we can efficiently determine the magnitude of the microlens parallax for high-magnification events.

The cheap-SPRX is "cheap" in two senses. First, as described in GY12, only two or three space-based observed data points are required to measure the microlens parallax. Second, this technique can be applied to only a small fraction of events (the total number of high-magnification events is inversely proportional to the peak magnification). Hence, if a satellite in solar orbit could be equipped with a camera and a means for prompt response for observations, it could carry out such a program at tiny additional cost to its principal mission.

GY12 discussed a potential application of the cheap-SPRX: to study planets through the high-magnification channel. High-magnification events are required for the cheap-SPRX, and they are a very important channel to discover planets because this channel provides almost 100 per cent detection efficiency if the events contain planetary mass companions to the lens stars (Griest & Safizadeh 1998). Based on these findings, GY12 argued that the cheap-SPRX could yield an unbiased measurement of the distribution of planets in the Galaxy.

However, since that time, a second major application has emerged: the mass function of isolated objects in the Galaxy (particularly, for low-mass objects). The masses of isolated objects can be measured only if the finite source effect is observed, i.e., if $u_0 \lesssim \rho_*$, where $\rho_* \equiv \theta_*/\theta_{\rm E}$ and θ_* is the angular radius of the source. This generally requires a high-magnification event (since ρ_* is typically $\mathcal{O}(10^{-3} - 10^{-2})$. This is the same condition necessary to measure the cheap-SPRX. Gould (1997) had already noted that high-magnification events could be used to yield isolated masses from a combination of finite source effects and the TPRX. Moreover, two cases were actually observed (Gould et al. 2009; Yee et al. 2009). Gould & Yee (2013) showed the number of these measurements should be $\propto n$, where n is the number density of objects, compared to the underlying microlensing event rate $\propto n\sqrt{M}$, where M is the lens mass. Hence, they are especially useful for measuring the mass function of low-mass objects because these are the most abundant objects in the Galaxy. However, as mentioned above, the chance of measuring such a TPRX is extremely low. Thus, in a practical sense, the study of isolated objects cannot be effectively carried out using the TPRX alone.

Compared to measurements of the TPRX, the SPRX can provide more robust opportunities to make the measurements. Actually, using *Spitzer* observations, Zhu et al. (2016) and Chung et al. (2017) found that a remarkably high fraction (3/170) of 2015 *Spitzer* targets yielded such isolated mass measurements. The principal reason is that *Spitzer* enables parallax measurements of much larger sources. For TPRX, by contrast, Gould & Yee (2013) showed that the maximum lens distance for which the method could be applied for large sources scales as $D_{\rm L} \propto \theta_*^{-1}$, implying that the available volume scales as θ_*^{-3}, thus virtually eliminating large sources for this method. These larger sources have a higher cross-section for crossing the lens, so a better chance of observing finite source effects[†] .

In fact, *Spitzer* itself is not well matched to the task of systematically measuring cheap-SPRX for high magnification events. *Spitzer* observations require long lead times (3 – 10 day delay between target selections and start of those observations, see Figure 1 of Udalski et al. 2015b), which raises the possibility of missing very short timescale events, which are most likely to be caused by the lowest mass objects. Moreover, *Spitzer* can observe the bulge only six weeks out of the eight month bulge season. In addition, the final campaign is currently scheduled to be in 2018.

As mentioned above, a systematic campaign to measure the cheap-SPRX could be conducted as an "add-on" capability to some future space mission. This would greatly increase the fraction of isolated objects characterized by microlensing. Based on this sample, we can determine the mass function of isolated objects at low cost. However, before pursuing such a course, we should perform a practical test of the cheap-SPRX idea to check the accuracy of the microlens parallax measurement. This test is important because the accuracy that can be achieved is directly related to establishing the feasibility of applying the cheap-SPRX under actual conditions and also for establishing an observational strategy for such a future, space-based microlensing campaign.

Here, we conduct the first practical test for the cheap-SPRX idea using the microlensing event OGLE-2016-BLG-1045 with *Spitzer* observations. In Section 2.1, we describe the event as a testbed for this practical test. In Section 2.2, we describe our method for testing the idea. Then, we present test results and our findings in Section 2.3. Lastly, we conclude and discuss in Section 3.

[†] Zhu et al. (2016) also noted that for standard SPRX, it is also more likely to see the finite source effect because there are two different observatory positions. However, this advantage is not relevant to cheap-SPRX.

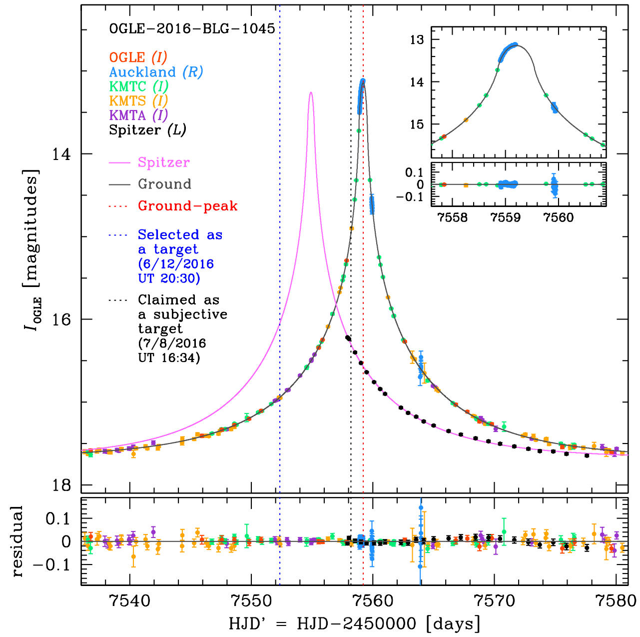

FIG. 1.— Light curves of the single-lens event OGLE-2016-BLG-1045 seen from the ground and space. Colored dots represent observed data taken from different telescopes located on the ground and in space (i.e., *Spitzer*). The dark gray and pink solid lines represent model light curves of the ground and *Spitzer*, respectively. The red dotted line indicates the peak time (t_0) of the ground-based light curve. The upper panel shows the observed light curves with their best-fit models. The lower panel shows residuals between the observations and the best-fit model. The inner panel shows the zoom-in of the peak part of ground-based light curve, which has a smooth feature due to the finite source effect.The dotted blue line indicates the time that this event was selected as a *Spitzer* target. The dotted black line indicates the time that the event was claimed as a *subjective* target.

2. TEST OF THE CHEAP-SPRX IDEA

2.1. *Testbed: OGLE-2016-BLG-1045 Spitzer event*

The microlensing event OGLE-2016-BLG-1045 occurred on a source that lies at $(\alpha,\delta)_{\rm J2000}$ = $(17^h36^m51^s.19, -34^\circ32'39''.7)$, which corresponds to the Galactic coordinates $(l,b) = (354.255, -1.386)$. The Optical Gravitational Lensing Experiment (OGLE: Udalski et al. 2015a) found this event and then the Early Warning System (Udalski et al. 1994; Udalski 2003) of the OGLE survey announced the event on 2016 June 9. The observations were made with the 1.3 m Warsaw telescope in the I−band channel of a 1.4 square-degree camera located at the Las Campanas

Observatory in Chile.

The event was highly magnified, implying that a planetary companion to the lens could probably be detected if it exists. Hence, a follow-up observation team called the Microlensing Follow-Up Network (μFUN: Gould et al. 2006) observed this event to capture any anomalies that might be produced by a planet. Auckland observatory, a μFUN member located in New Zealand, made the observations with a 0.4 m telescope using a number 12 Wratten filter (which is similar to R–band). The Auckland observations successfully covered the peak of the event. This peak coverage did not reveal an anomaly in the light curve due to a planetary lens system. However, the good coverage of the peak provided a chance to detect the finite source effect, which enters the determination of the angular Einstein ring radius, i.e., $\rho_* = \theta_*/\theta_{\rm E}$.

There exist other μFUN observations in H–band taken at the Cerro Tololo International Observatory in Chile with the 1.3 m SMARTS telescope (CTIO). These CTIO data were not included in the final models, but were used for the color-magnitude diagram (CMD) analysis of the event (see Appendix).

The Korea Microlensing Telescope Network (KMTNet: Kim et al. 2016) also observed this event. Three identical 1.6 m telescopes located in the Cerro Tololo International Observatory in Chile (KMTC), the South African Astronomical Observatory in South Africa (KMTS), and the Siding Spring Observatory in Australia (KMTA) observed this event with the I–band channel of their 4 deg^2 cameras. The KMTNet observations provided overall coverage of the light curve.

This event was *secretly* chosen as a target of the 2016 *Spitzer Microlensing Campaign* on 2016 June 16 (UT 20:30) based on the possibility that the event could be highly magnified. The event was later claimed as a "subjective" target on 2016 June 18 (UT 16:34) once the event was observed to be moderate to high magnification (see Yee et al. 2015b for more details on different types of event selection). The observations began on 2016 June 18 (UT 9:56) and ended on July 8 (UT 2:43). The *Spitzer Space Telescope* took 24 total data points over 20 days with the 3.6 μm channel (L–band) of the IRAC camera.

The observed data sets were reduced by each group using their own pipelines and difference-imaging analysis packages: [(OGLE (DIA): Alard & Lupton 1998; Wozniak 2000), (μFUN and KMTNet (pySIS): Albrow et al. 2009). The *Spitzer* data were reduced with point response function photometry (Calchi Novati et al. 2015b).

In Figure 1, we present light curves of the event observed from ground and space. The ground-based light curve shows a symmetric Paczyński curve with a smooth peak feature, which implies that the event was produced by single lens affected by the finite source effect. The *Spitzer* observations only partially covered the light curve. However, Han et al. (2017), Shin et al. (2017), and Wang et al. (2017) already showed that it is possible to accurately measure the SPRX even though the space-based observations are fragmentary. Thus, for this event, using the *Spitzer* observations and the finite source effect, it is possible to measure the microlens parallax and the angular Einstein ring radius, which yield the properties of the isolated lens.

The *Spitzer* observations were not taken with the idea of "cheap-SPRX" in mind. In fact, because the peak magnification was relatively unconstrained when the observations were scheduled, many similar events were observed on the chance that one of them would be high-magnification (so, these observations cannot be considered "cheap"). Nevertheless, the resulting observations contain what would be obtained for a "cheap-SPRX" campaign, i.e., the *Spitzer* observations exist near the peak of the ground-based light curve and also exist near the baseline. Hence, this event can serve as an excellent testbed to perform a practical test of the cheap-SPRX idea.

TABLE 1
LIMB-DARKENING COEFFICIENTS AND ERROR RE-SCALING FACTORS

Observations	Γ_λ	k
OGLE (I)	0.5103	0.913
Auckland (R)†	0.6583	2.370
KMTC (I)	0.5103	1.116
KMTS (I)	0.5103	1.501
KMTA (I)	0.5103	1.446

NOTE. — †We use a modified LD coefficient for Auckland observations, $\Gamma_R = (\Gamma_R + \Gamma_V)/2 = (0.61118 + 0.7048)/2 = 0.6583$ because the Auckland observatory used a 12 Wratten filter having a flat transmission between 540 – 700 nm. Thus, the filter is similar to the mean value of R– and V–bands. Note that we did not use a Γ_L because it plays no role for the *Spitzer* observations.

2.2. *Test Method*

To test the accuracy of the cheap-SPRX method, we test three cases using the *Spitzer* data and compare with the SPRX measurements. In order of information (most to least), these are the "Actual", "Realistic", and "Idealized" cases. We first consider the two extremes, which are the "Actual" case defined by the current experiment and the "Idealized" GY12 case. For the "Actual" case, we use all observed *Spitzer* data (24 points). From this case, we can obtain the *actual* SPRX measurement that can be used as a reference to compare with the measurements derived from the other cases. For the "Idealized" case, considering the *ideal* situation proposed by GY12, this represents the minimum amount of data necessary for the cheap-SPRX idea to work. For this case, we generate two artificial data points using the *Spitzer* data and the best-fit model light curve. One is located at the exact ground-based peak (HJD$'$ = 7559.201) and the other is located at the baseline (HJD$'$ = 7900.000). For the "Realistic" case, we choose two actual data points near the ground-based peak (HJD$'$ = 7559.172 and 7559.482) because it is almost impossible to take an image at the exact peak time in realistic situations. In addition, we use the last point (HJD$'$ = 7577.613) observed by *Spitzer*, which is located near the baseline. Based on these selected *Spitzer* data, we can obtain a measurement of the cheap-SPRX under *realistic* conditions. In Figure 2, we present light curves of the cases that clearly show the space-based observations used for the test.

Based on the three cases, we conduct modeling to measure the SPRX value of each case. For the modeling, we use six parameters: (t_0, u_0, t_E, ρ_*, $\pi_{\rm E}$, and Φ). Among them, three basic parameters (t_0, u_0, and t_E) describe the light curve produced by a single-lens and a point-source. These basic parameters are closely related to each other: t_0 is the time at the peak of the light curve; u_0 is the impact parameter, i.e., the separation

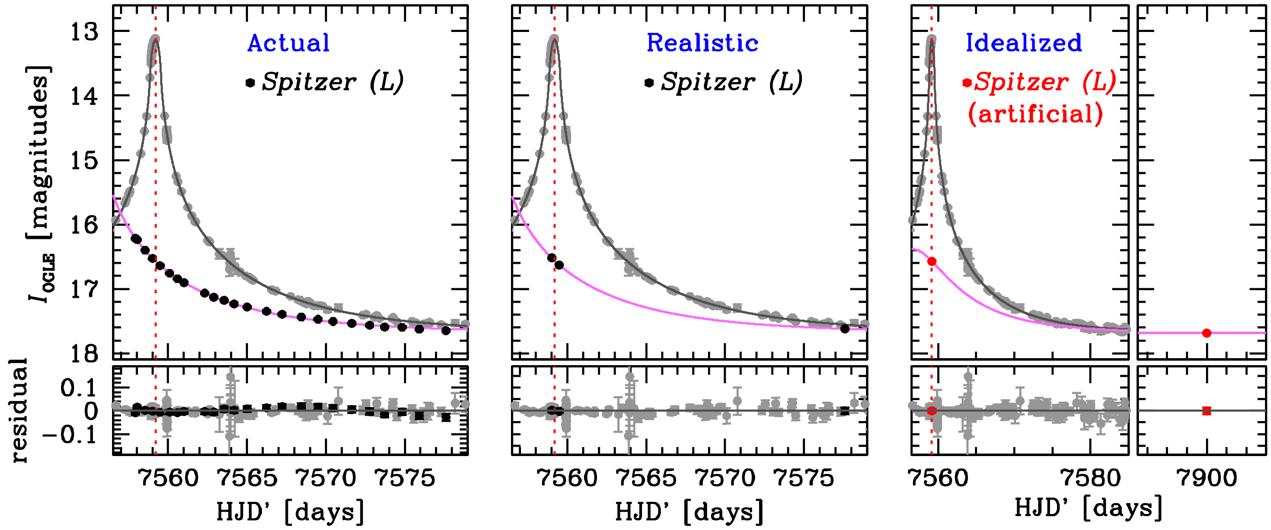

FIG. 2.— Light curves showing each test case. The left panel shows the "Actual" case using all actually observed 24 *Spitzer* data points. The middle panel shows the "Realistic" case using 3 selected *Spitzer* data points considering realistic space-based observations of the cheap-SPRX idea. The right panel shows the "Idealized" case using 2 artificial data points considering the ideal situation of the cheap-SPRX idea. The gray, black, and red dots indicate ground-based observations, *Spitzer* observations, and the artificial data, respectively. Black and magenta lines represent the best-fit model light curves of (−,+) solutions of each case.

TABLE 2
THE BEST-FIT MODEL WITH DEGENERATE SOLUTIONS OF EACH CASE

Case	Actual		Realistic		Idealized	
parameter	(−,+)	(+,+)	(−,+)	(+,+)	(−,+)	(+,+)
$\chi^2_{\rm total}$	1368.70 / 1372	1368.99 / 1372	1344.89 / 1351	1345.04 / 1351	1343.83 / 1350	1343.95 / 1350
$\chi^2_{\rm Ground}$	1345.01 / 1348	1345.09 / 1348	1344.77 / 1348	1344.77 / 1348	1343.83 / 1348	1343.95 / 1348
$\chi^2_{Spitzer}$	23.69 / 24	23.90 / 24	0.12 / 3	0.27 / 3	0.00 / 2	0.00 / 2
$\chi^2_{\rm penalty}$	0.017	0.075	0.000	0.010	0.003	0.014
$(I-L)$ [3.80]	3.797	3.794	3.800	3.802	3.799	3.803
t_0 (HJD')	7559.201±0.001	7559.201±0.001	7559.201±0.001	7559.201±0.001	7559.202±0.001	7559.202±0.001
u_0 (10^{-2})	-1.308±0.038	1.314±0.039	-1.318±0.038	1.318±0.039	-1.312±0.038	1.309±0.039
$t_{\rm E}$ (days)	11.981±0.082	11.963±0.084	11.950±0.082	11.947±0.083	11.956±0.083	11.952±0.083
ρ_* (10^{-2})	3.186±0.029	3.190±0.030	3.195±0.029	3.195±0.030	3.194±0.029	3.193±0.029
$\pi_{\rm E}$	0.355±0.005	0.352±0.005	0.355±0.007	0.350±0.007	0.365±0.009	0.346±0.009
Φ (radian)	1.291±0.106	1.353±0.109	1.210±0.310	1.178±0.307	0.341±1.220	0.407±1.238
$\pi_{{\rm E},E}$	0.341±0.009	0.344±0.010	0.332±0.032	0.323±0.032	0.122±0.225	0.137±0.232
$\pi_{{\rm E},N}$	0.098±0.037	0.076±0.038	0.125±0.102	0.134±0.101	0.344±0.207	0.317±0.201
$F_{\rm S,OGLE}$	1.370±0.012	1.373±0.012	1.375±0.012	1.375±0.012	1.374±0.012	1.374±0.012
$F_{\rm B,OGLE}$	-0.032±0.012	-0.034±0.012	-0.036±0.012	-0.037±0.012	-0.035±0.012	-0.036±0.012
$F_{{\rm S},Spitzer}$	45.257±0.923	45.212±0.948	45.518±1.016	45.622±1.069	45.439±1.035	45.618±1.055
$F_{{\rm B},Spitzer}$	-6.528±0.975	-6.430±0.996	-8.032±1.044	-8.179±1.098	-6.674±1.035	-6.854±1.055

NOTE. — HJD′ = HJD − 2450000.0. We note that the $\pi_{{\rm E},E}$ and $\pi_{{\rm E},E}$ are not modeling parameters. These are calculated from the modeling parameters, $\pi_{\rm E}$ and Φ. We also note that units of all fluxes are normalized at I = 18.0 using the OGLE source of this event.

between the center of the Einstein ring and the position of the source at time t_0; $t_{\rm E}$ is the crossing-time of the Einstein ring. Another parameter ρ_* is the angular source radius (θ_*) normalized by the angular Einstein ring radius ($\theta_{\rm E}$), $\rho_* \equiv \theta_*/\theta_{\rm E}$, which describes the finite source effect. The last two parameters ($\pi_{\rm E}$ and Φ) describe the SPRX, which differs from the conventional way of describing the microlens parallax vector $\boldsymbol{\pi}$ (normally consisting of North ($\pi_{{\rm E},N}$) and East ($\pi_{{\rm E},E}$) components). In our parameterization (see also Bennett et al. 2008),

$$\boldsymbol{\pi}_{\rm E} = (\pi_{{\rm E},N}, \pi_{{\rm E},E}) \rightarrow (\pi_{\rm E}\cos\Phi, \pi_{\rm E}\sin\Phi). \qquad (6)$$

The Φ angle is allowed to vary over the full possible range $[-\pi, +\pi]$[‡]. In addition, there are flux parameters (F_S and F_B) for each data set that describe the fluxes of the source and blend, respectively, which are fit linearly for each model. Using these parameters, we search for the best-fit model with the minimum χ^2 between the observed and modeled light curves using Markov Chain Monte Carlo (MCMC) χ^2 minimization.

During the modeling process, we consider the limb-darkening (LD) of the source star. We adopt LD coefficients for observed passbands from Claret (2000) based on the spectral source type determined by the CMD analysis (described in the Appendix). In addition, we re-scale the errors of observations to enforce $\chi^2/{\rm dof} \simeq 1$ using the equation $e_{\rm new} = k(e_{\rm old})$

[‡] The parameter Φ is treated as a cyclic variable. That is, whenever it crosses the "boundaries" at $\pm\pi$, its formal value is changed by $\mp 2\pi$, so that there are no rejected links due to these "boundaries".

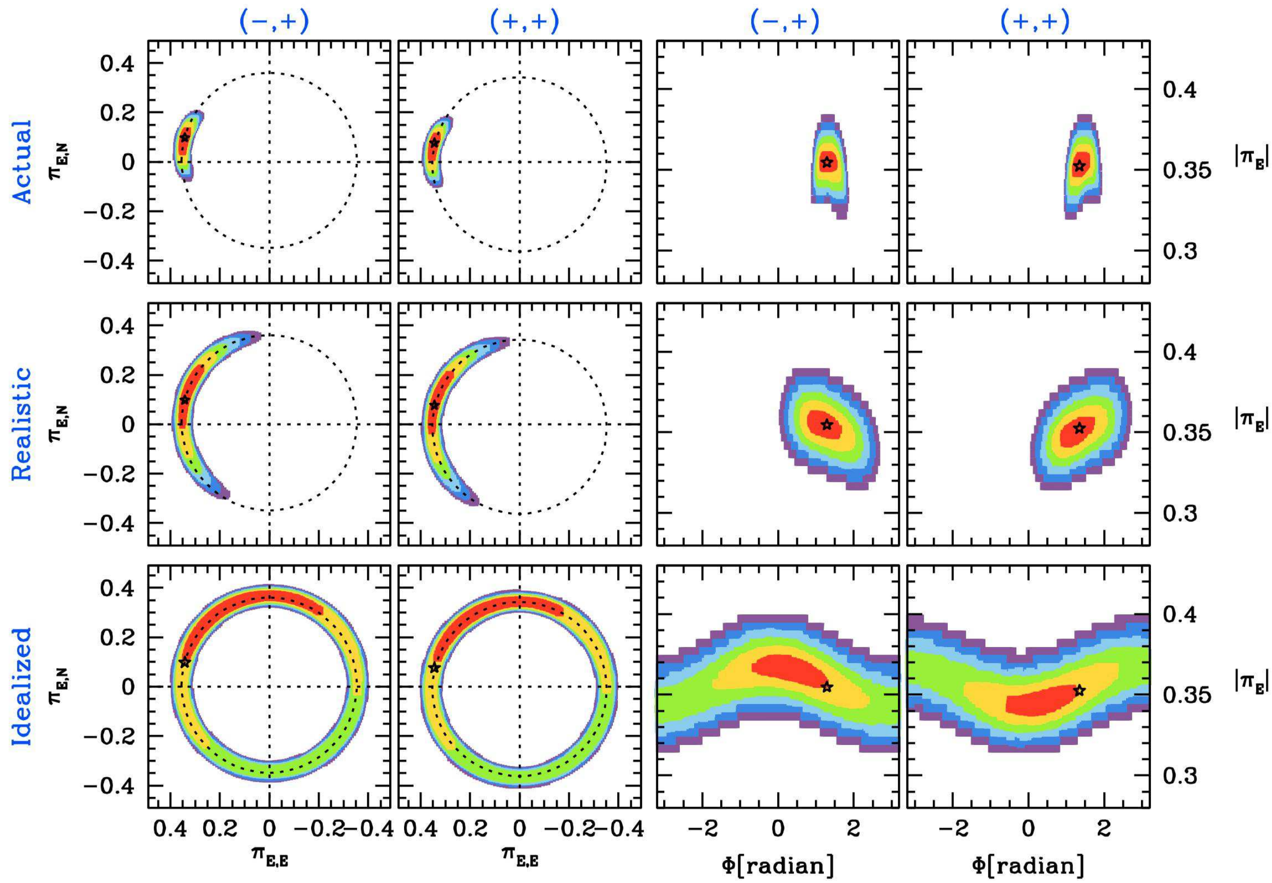

FIG. 3.— The SPRX distributions of each case with degenerate solutions. The top, middle, and bottom panels show the SPRX distributions of the actual, realistic, and idealized cases, respectively. The left six panels present the ($\pi_{{\rm E},E}$, $\pi_{{\rm E},N}$) distributions according to the conventional parameterization. The right six panels present the ($\pi_{\rm E}$, Φ) distributions that are the MCMC parameters used to describe the SPRX. The red, yellow, green, light blue, blue, and purple colors represent $\Delta\chi^2 = 1^2, 2^2, 3^2, 4^2, 5^2$, and 6^2, respectively. The star symbols indicate the best-fitted SPRX value of the actual case.

where k is the error re-scaling factor.

We also incorporate the color-constraint, $(I-L) = 3.800 \pm 0.020$, which provides an independent constraint on the model. The constraint is determined using I–band ground observations (OGLE) and L–band space observations (*Spitzer*) based on the CMD analysis. To incorporate the $(I-L)$ color-constraint, we introduce $\chi^2_{\rm penalty}$ described in Section 3.2 of Shin et al. (2017). The $\chi^2_{\rm penalty}$ increases the χ^2 when the fitted $(I-L)$ color of the model is different from the constraint. In particular, the $\chi^2_{\rm penalty}$ increases strongly when the difference between the fitted color and the constraint is larger than 2σ. In Table 1, we present these LD coefficients and error re-scaling factors for modeling.

In Table 2, we present the best-fit parameters for each case. For each case, we find that there exist two degenerate solutions due to the "four-fold degeneracy" (Refsdal 1966; Gould 1994). In principle, the four-fold degeneracy has four solutions, (+,+), (+,−), (−,+), and (−,−) (denoted according to the convention described in Zhu et al. 2015), which are caused by different pairs of source trajectories (seen by ground and space) that travel over a similar lensing magnification pattern. However, for this event, we find that there exist only two solutions, (−,+) and (+,+) because the remaining two solutions, (−,−) and (+,−), are merged with the (−,+) and (+,+) solutions, respectively. Uncertainties of these parameters are determined based on the 68% confidence intervals of the MCMC chains.

TABLE 3
PHYSICAL PROPERTIES OF THE LENS FOR EACH CASE

		$M_{\rm L}$ [$M_\odot$]	$D_{\rm L}$ [kpc]
Actual	(−,+)	0.085±0.005	5.012±0.473
	(+,+)	0.085±0.005	5.028±0.476
Realistic	(−,+)	0.084±0.005	5.018±0.475
	(+,+)	0.086±0.006	5.048±0.480
Idealized	(−,+)	0.082±0.005	4.952±0.465
	(+,+)	0.087±0.006	5.073±0.486

2.3. *Test Results*

In Figure 3, we present the SPRX distributions of each case. The distributions are constructed from the MCMC chains. These distributions clearly show the consistency of the SPRX measurements. We present two types of distributions. One type of distribution is presented according to the conventional parameters, $(\pi_{{\rm E},E}, \pi_{{\rm E},N})$, which are calculated from the MCMC parameters as $\pi_{{\rm E},E} = \pi_{\rm E} \sin\Phi$ and $\pi_{{\rm E},N} = \pi_{\rm E}\cos\Phi$. The other is the ($\pi_{\rm E}$, Φ) distribution, which can be used to directly check the accuracy of the magnitude of the SPRX measurement.

From the modeling of the actual case, we obtain the SPRX measurements for the (−,+) and (+,+) cases: $\pi_{\rm E} = 0.3547 \pm 0.0049$ and $\pi_{\rm E} = 0.3524 \pm 0.0053$, respectively. We find that the magnitudes of the SPRX values between the (−,+) and

(+,+) solutions of the actual case are consistent to well within 1σ. Based on the actual SPRX measurements, we can compare the other test cases of the cheap-SPRX idea to check the accuracy of the cheap-SPRX measurements. For the realistic case, we find that the SPRX measurements of both degenerate solutions, 0.3547 ± 0.0065 and 0.3498 ± 0.0069, are consistent with those of the actual case to within 1σ. For the idealized case, the measurements, 0.3654 ± 0.0092 and 0.3456 ± 0.0090, are consistent with those of the actual case to within 2σ using the actual-case errors and to within $\lesssim 1\sigma$ using the idealized-case errors.

Based on the SPRX measurements, we can determine the properties of this isolated lens by combining it with the angular Einstein ring radius ($\theta_{\rm E} = \theta_*/\rho_*$), where θ_* is the angular source radius determined from the CMD analysis (described in the Appendix) and ρ_* is determined from the finite source effect. We determine the angular Einstein ring radius as

$$\theta_{\rm E} = 0.245 \pm 0.015\,{\rm mas}. \qquad (7)$$

We also determine the physical properties of the lens, i.e., the lens mass ($M_{\rm L}$) and the lens distance ($D_{\rm L}$), using Equation (2) and

$$M_{\rm L} = \frac{\theta_{\rm E}}{\kappa\pi_{\rm E}}, \quad \kappa = 8.14\,{\rm mas}M_\odot^{-1}, \qquad (8)$$

$$D_{\rm L} = \frac{\rm au}{\pi_{\rm E}\theta_{\rm E} + \pi_S}, \quad \pi_S = \frac{\rm au}{D_S}, \qquad (9)$$

where D_S is the distance to the source estimated from Nataf et al. (2013). For this event, the estimated D_S is ~ 8.87 kpc.

In Table 3, we present the lens properties determined from each case. From the results, we find that all properties are consistent to within 1σ. This fact implies that the accuracy of the SPRX measurement based on the cheap-SPRX idea is sufficient to accurately determine the properties of the isolated object.

3. CONCLUSION AND DISCUSSION

Based on the event OGLE-2016-BLG-1045, we tested the cheap-SPRX idea to check the accuracy of the microlens parallax measurement by comparing it to the true measurement. In addition, based on the parallax measurement of each case, we checked whether the physical properties of this isolated lens are consistent or not. We found that the magnitudes of the actual SPRX measurement and the realistic, cheap-SPRX measurement are consistent to within 1σ. We also found that the lens mass determined for all cases is consistent ~ 0.08 $M_\odot$, which is the upper-mass limit for brown dwarfs. In addition, the lens distances derived for all cases are also consistent to within 1σ. Hence, we conclude that the cheap-SPRX measurement has sufficient accuracy to adopt this idea in real situations. Thus, using only 2 or 3 space-based observations, we can determine the physical properties of the lens for high-magnification events. This fact implies that by adopting the cheap-SPRX idea, we have a robust method of measuring microlens parallaxes (i.e., SPRX), which can reveal the nature of the lens with a cost-effective space-based campaign.

A space-based microlensing campaign, perhaps added on to another mission, adopting this cost-effective idea can provide a measurement of the magnitude of the microlens parallax for most high-magnification events. This complete sample can be used to study isolated objects, especially low-mass objects, in the Galaxy and derive a mass function based on them.

This research has made use of the KMTNet system operated by the Korea Astronomy and Space Science Institute (KASI) and the data were obtained at three host sites of CTIO in Chile, SAAO in South Africa, and SSO in Australia. This work is based in part on observations made with the Spitzer Space Telescope, which is operated by the Jet Propulsion Laboratory, California Institute of Technology under a contract with NASA. OGLE project has received funding from the National Science Centre, Poland, grant MAESTRO 2014/14/A/ST9/00121 to A. Udalski. Work by I-G. Shin and A. Gould was supported by JPL grant 1500811. A. Gould, Y. K. Jung, and W. Zhu acknowledges the support from NSF grant AST-1516842. Work by YS and CBH was supported by an appointment to the NASA Postdoctoral Program at the Jet Propulsion Laboratory, administered by Universities Space Research Association through a contract with NASA. Work by C.H. was supported by the grant (2017R1A4A1015178) of National Research Foundation of Korea

APPENDIX

THE COLOR-MAGNITUDE DIAGRAM (CMD) ANALYSIS

From this CMD analysis, we can determine the angular source radius, the spectral type of the source star, and the model-independent color constraint. The CMD analysis is usually conducted by combining the $(V-I, I)$ CMD and the standard method (Yoo et al. 2004). However, for this event, the source is severely extincted with $A_I \sim 3.5$ in I−band. As a result, the standard method cannot be applied using the $(V-I, I)$ CMD. Hence, we construct a new $(I-H, I)$ CMD based on the OGLE survey and the VISTA Variables and Via Lactea Survey (VVV: Minniti et al. 2010) using cross-matching of stars.

In Figure 4, we present the $(I-H, I)$ CMD. Based on the CMD, we conduct the CMD analysis using the standard method. First, we determine the location of the centroid of the giant clump on the CMD as $(I-H, I)_{\rm C} = (4.00 \pm 0.03, 18.25 \pm 0.05)$. Second, the location of the source on the CMD is determined based on source fluxes in I band and H band from the best-fit model additionally including CTIO H−band data. The magnitudes are found to be $I_{S,{\rm OGLE}} = 17.658 \pm 0.004$ and $H_{S,{\rm CTIO}} = 17.648 \pm 0.003$. The CTIO H−magnitude scale is converted to the VVV H−magnitude scale using the relation $(H_{\rm CTIO} - H_{\rm VVV})_{\rm S} = 4.0587 \pm 0.0114$, which comes from comparison stars. Thus, the location of the source on the CMD is determined to be $(I-H, I)_{\rm S} = (4.068 \pm 0.012, 17.658 \pm 0.004)$.

We adopt the de-reddened color (Bensby et al. 2013) and intrinsic magnitude (Nataf et al. 2013) of the giant clump as a reference. The adopted values are $(V-I, I)_{0,{\rm C}} = (1.06 \pm 0.01, 14.62 \pm 0.04)$. Based on this reference, we can obtain the de-reddened color and magnitude of the source under the assumption that the clump and source experience the same extinction. In addition, the $(I-H)$ color is converted to the $(V-I)$ color using the color-color relation in Bessell & Brett (1988). For the source of this event, the relation is $\Delta(I-H) = 1.00 \times \Delta(V-I)$. Thus, the de-reddened color and magnitude of the source are $(V-I)_{0,{\rm S}} = (V-I)_{0,{\rm C}} - [(I-H)_{\rm C} - (I-H)_{\rm S}]$ and $I_{0,{\rm S}} = I_{0,{\rm C}} - [I_{\rm C} - I_{\rm S}]$, respectively. Lastly, we obtain the de-reddened color and

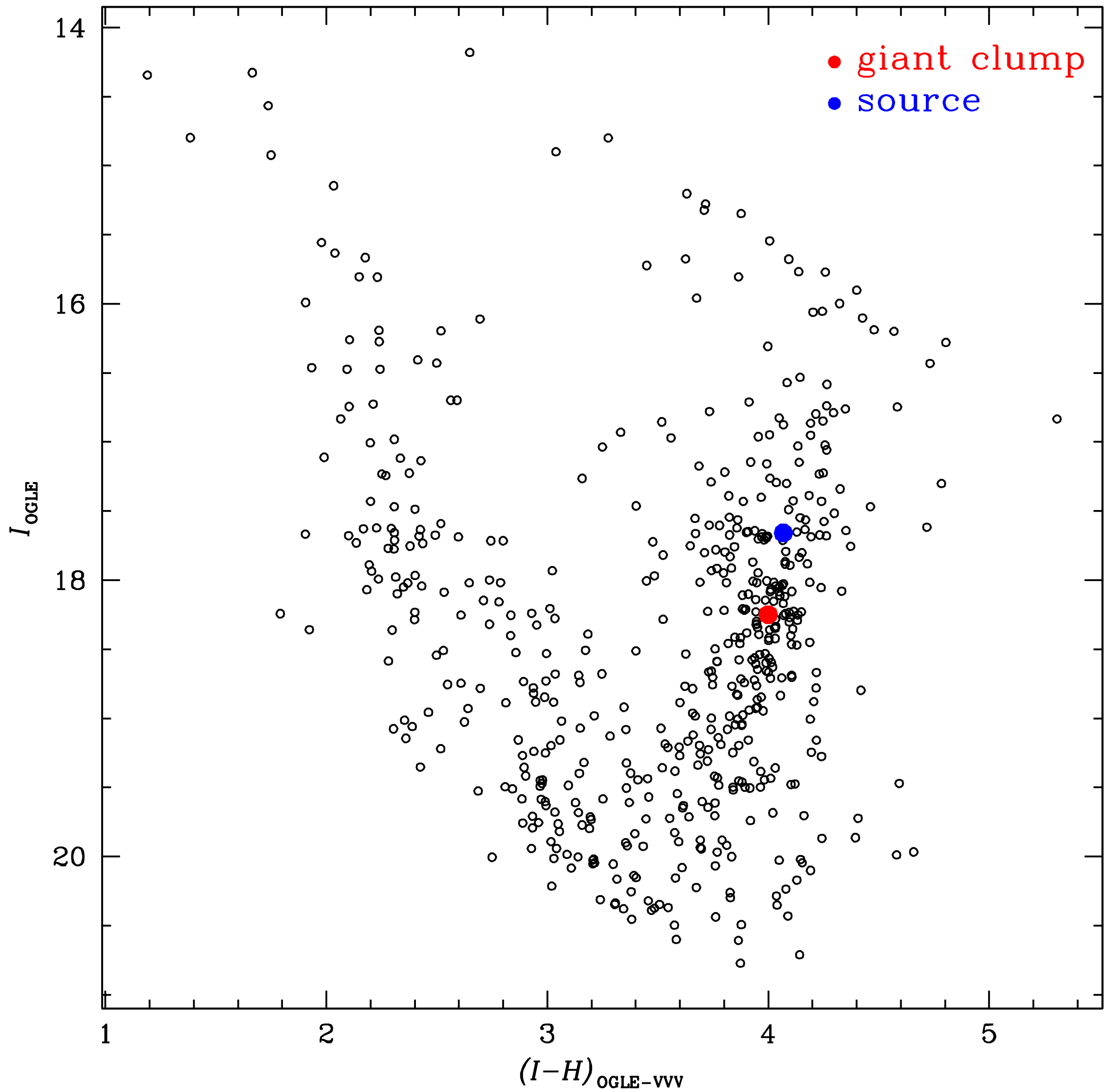

FIG. 4.— The $(I-H,I)$ CMD of the OGLE-2016-BLG-1045 event. The CMD is constructed by cross-matching OGLE and VVV observations. The red and blue dots indicate the centroid of the giant clump and the source, respectively.

magnitude of the source: $(V-I,I)_{0,\rm S} = (1.128 \pm 0.034, 14.028 \pm 0.064)$.

From the color of the source, we determine the angular source radius using the color/surface-brightness relations in Kervella et al. (2004). To employ the relation, we convert the $(V-I)_{0,\rm S}$ to $(V-I)_{0,\rm S}$ by using the Bessell & Brett (1988) relation. The determined angular source radius is

$$\theta_* = 7.80 \pm 0.47 \ \text{uas}. \tag{A1}$$

Moreover, based on the intrinsic source color, we estimate the source star to be an early K-type giant. We adopt LD coefficients from Claret (2000) assuming typical properties of an early K-type giant: effective temperature $T_{\rm eff} \simeq 4750$ K, surface gravity $\log g \simeq 2.0$, microturbulent velocity $V_t \simeq 2.0 \ {\rm km\,s^{-1}}$, and metallicity $\log{[M/H]} \simeq 0.0$. The adopted LD coefficients are presented in Table 1.

Based on the information of the source, we determine the $(I-L)$ color constraint using the color-color regression method based on the IHL color-color diagram. This process is described in Calchi Novati et al. (2015b) and Shin et al. (2017). The determined $(I-L)$ color constraint is

$$(I-L) = 3.800 \pm 0.020. \tag{A2}$$

We incorporate this model-independent constraint in the modeling process by introducing an additional $\chi^2_{\rm penalty}$, which increases as $\Delta(I-L)$ increases between the color calculated from the model and the constraint.

REFERENCES

Alard, C. & Lupton, Robert H. 1998, ApJ, 503, 325
Albrow, M. D., Horne, K., Bramich, D. M., et al. 2009, MNRAS, 397, 2099
Barclay, T., Quintana, E. V., Raymond, S. N., & Penny, M. T. 2017, ApJ, 841, 86

Bennett, D.P., Bond, I.A., Udalski, A., et al. 2008, ApJ, 684, 663
Bensby, T., Yee, J. C., Feltzing, S., et al. 2013, A&A, 549, 147
Bessell, M. S., & Brett, J. M. 1988, PASP, 100, 1134
Bihain, G., Rebolo, R., Zapatero Osorio, M. R., et al. 2009, A&A, 506, 1169
Bozza, V., Shvartzvald, Y., Udalski, A., et al. 2016, ApJ, 820, 79
Calchi Novati, S., Gould, A., Udalski, A., et al. 2015, ApJ, 804, 20
Calchi Novati, S., Gould, A., Yee, J. C., et al. 2015, ApJ, 814, 92
Chatterjee, S., Ford, E. B., Matsumura, S., & Rasio, F. A. 2008, ApJ, 686, 580
Chung, S.-J., Zhu, W., Udalski, A., et al. 2017, ApJ, 838, 154
Claret, A. 2000, A&A, 363, 1081
Dong, S., Udalski, A., Gould, A., et al. 2007, ApJ, 664, 862
Esplin, T. L., & Luhman, K. L. 2017, AJ, 154, 134
Fryer, C. L., Belczynski, K., Wiktorowicz, G., et al. 2012, ApJ, 749, 91
Gould, A. 1992, ApJ, 392, 442
Gould, A. 1994, ApJ, 421, L75
Gould, A. 1997, ApJ, 480, 188
Gould, A., Dong, S., Bennett, D. P., et al. 2010, ApJ, 710, 1800
Gould, A., Udalski, A., An, D., et al. 2006, ApJ, 644, L37
Gould, A., Udalski, A., Monard, B., et al. 2009, ApJ, 698, L147
Gould, A., & Yee, J. C. 2012, ApJ, 755, L17
Gould, A., & Yee, J. C. 2013, ApJ, 764, 107
Griest, K., & Safizadeh, N. 1998, ApJ, 500, 37
Han, C., Udalski, A., Gould, A., et al. 2016, ApJ, 828, 53
Han, C., Udalski, A., Gould, A., et al. 2017, ApJ, 834, 82
Jurić, M., & Tremaine, S. 2008, ApJ, 686, 603
Kervella, P., Bersier, D., Mourard, D., et al. 2004, A&A, 428, 587
Kim, S.-L., Lee, C.-U., Park, B.-G., et al. 2016, JKAS, 49, 37
Minniti, D., Lucas, P. W., Emerson, J. P., et al. 2010, NewA, 15, 433
Mróz, P., Udalski, A., Skowron, J., et al. 2017, Nature, 548, 183
Mróz, P. Ryu, Y.-H., Skowron, J., et al. 2017b, arXiv:1712.01042
Nataf, D. M., Gould, A., Fouqué, P., et al. 2013, ApJ, 769, 88
Özel, F., Psaltis, D., Narayan, R., & Santos Villarreal, A. 2012, ApJ, 757, 55
Poleski, R., Zhu, W., Christie, G. W., et al. 2016, ApJ, 823, 63
Refsdal, S. 1966, MNRAS, 134, 315
Ryu, Y.-H., Yee, J.C., Udalski, A. et al. 2017, AJ, in press, arXiv:1710.09974
Shin, I.-G., Udalski, A., Yee, J. C., et al. 2017, AJ, 154, 176
Shvartzvald, Y., Li, Z., Udalski, A., et al. 2016, ApJ, 831, 183
Shvartzvald, Y., Udalski, A., Gould, A., et al. 2015, ApJ, 814, 111
Shvartzvald, Y., Yee, J. C., Calchi Novati, S., et al. 2017, ApJ, 840, L3
Street, R. A., Udalski, A., Calchi Novati, S., et al. 2016, ApJ, 819, 93
Sumi, T., Kamiya, K., Bennett, D. P., et al. 2011, Nature, 473, 349
Udalski, A. 2003, Acta Astron., 53, 291
Udalski, A., Szymański, M., Kaluzny, J., et al. 1994, Acta Astron., 44, 227
Udalski, A., Szymański, M. K., Szymański, G. 2015, Acta Astron., 65, 1
Udalski, A., Yee, J. C., Gould, A., et al. 2015, ApJ, 799, 237
Wang, T., Zhu, W., Mao, S., et al. 2017, ApJ, 845, 129
Wozniak, P. R. 2000, Acta Astron., 50, 421
Whitworth A., Bate M. R., Nordlund Å., Reipurth B., Zinnecker H., 2007, in Reipurth B., Jewitt D., Keil K., eds, Protostars and Planets V. Tucson, University of Arizona Press, p. 459
Yee, J. C., Gould, A., Beichman, C., et al. 2015, ApJ, 810, 155
Yee, J. C., Udalski, A., Calchi Novati, S., et al. 2015, ApJ, 802, 76
Yee, J. C., Udalski, A., Sumi, T., et al. 2009, ApJ, 703, 2082
Yoo, Jaiyul, DePoy, D. L., Gal-Yam, A., et al. 2004, ApJ, 603, 139
Zhu, W., Calchi Novati, S., Gould, A., et al. 2016, ApJ, 825, 60
Zhu, W., Udalski, A., Calchi Novati, S., et al. 2017, AJ, 154, 210
Zhu, W., Udalski, A., Gould, A., et al. 2015, ApJ, 805, 8